



Solid-to-super-critical phase change and resulting stress wave during internal laser ablation

Yan Li, Chong Li, Wenlong Yao & Xinwei Wang

To cite this article: Yan Li, Chong Li, Wenlong Yao & Xinwei Wang (2018) Solid-to-super-critical phase change and resulting stress wave during internal laser ablation, Journal of Thermal Stresses, 41:10-12, 1364-1379

To link to this article: <https://doi.org/10.1080/01495739.2018.1490634>



Published online: 12 Feb 2019.



Submit your article to this journal [↗](#)




View Crossmark data [↗](#)

SPECIAL ISSUE TO COMMEMORATE THE 90TH BIRTHDAY OF RICHARD B. HETNARSKI
AND 40 YEARS OF THE *JOURNAL OF THERMAL STRESSES*



Solid-to-super-critical phase change and resulting stress wave during internal laser ablation

Yan Li^{a,b}, Chong Li^b, Wenlong Yao^a, and Xinwei Wang^b 

^aDepartment of Mechanical Engineering, Ocean University of China, Qingdao, P.R. China; ^bDepartment of Mechanical Engineering, Iowa State University, Ames, IA, USA

ABSTRACT

The phase change, stress wave generation and propagation, and stress-induced structure damage in a model material (argon) during internal picosecond laser ablation are studied by molecular dynamic simulations. The propagation of the stress wave and fluctuations in temperature is periodic and tightly correlated. The phase-change process from solid to liquid and supercritical fluid and then back to solid occurs as a coupled consequence of heat transfer and the tensile stress wave induced by the laser pulse and the limited internal space. The orientation–radial distribution function is applied to provide substantial information about the atomic density and angle distribution of the crystal structure. It reveals the strong material twisting and permanent damaged region induced by the very high stress fields.

ARTICLE HISTORY



Received 20 April 2018
Accepted 15 June 2018

KEYWORDS

Laser-ablation; molecular dynamics; phase change; stress wave; super critical fluid; temperature fluctuation

Introduction

Pulsed laser ablation leads to very strong local structure change of a material [1, 2]. Lasers with very short pulse durations in the order of femtoseconds or picoseconds are promising in many applications [3]. The basic mechanisms of the involved laser–material interaction have been studied using molecular dynamic (MD) simulations [4, 5]. Picosecond laser processing is characterized by small spatial and temporal scales and by complex processes of thermodynamics, optics, energy transfer, and mechanics. The thermal and mechanical properties of materials under extremely high temperatures and pressures are usually unknown. The high energy and short pulses cause the near-surface area to suddenly become a mixture of vapor and equilibrium liquid droplets. This process is called phase explosion [6]. Song and Xu [7] used nickel as a specimen to study the laser fluence threshold of phase explosion. The solid material can be directly heated to a temperature above the critical temperature, followed by expansion that leads to a thermodynamically unstable region, causing material decomposition [8]. This material decomposition process from solid to supercritical fluid and then to an unstable region is termed critical-point phase separation [4]. Experimental and numerical research of the phase-change process during nanosecond and picosecond laser ablation has been carried out by many groups [5, 7, 9–13]. The phase-change phenomena induced by femtosecond laser pulses have also been studied, including the generation of the vapor phase in the superheated liquid and the determination of the transient temperature and the time required to form the two-phase mixture [14].

CONTACT Xinwei Wang  xwang3@iastate.edu  Department of Mechanical Engineering, Iowa State University, Ames, IA 50011, USA.

Color versions of one or more of the figures in the article can be found online at www.tandfonline.com/uths.

Nanostructure fabrication is a typical application of laser–material interactions. Nanostructures can be formed inside a photosensitive glass using a focused femtosecond laser [15, 16]. The discovery of long-range, self-organized, periodic planar nanocrack structures in fused silica is an important development in the field of laser dielectric modification [17]. Techniques for two-dimensional (2D) or three-dimensional (3D) image engraving inside a crystal have been developed on the basis of fused silica’s transparency and high refractive index [18, 19]. Ionization owing to multiphoton and avalanche processes increases the absorption in the localized area of the optical breakdown [20]. As a result of the laser energy absorption, the matter inside the breakdown area is heated and the process chain is triggered.

The study of internal laser ablation using MD simulation is relatively rare. The internal ablation process is very difficult to study because many of the experimental techniques cannot reach the internal material to measure the temperature, stress, and other properties. Experiments and computer simulations by the Quéré [21] and Bulgakova [22] groups include 3D patterning of the developing optical breakdown in transparent solids. In their experiments, the subpicosecond evolution of breakdown development is probed using the pump–probe technique. In addition, internal ablation has very different characteristics from open-space ablation because the material’s phase change is extremely confined by the solid material surrounding it. The constraint in open space has been studied by Wang’s group [23–25]. The laser–material interaction in the presence of ambient gas leads to the formation of a shock wave, which can substantially affect the phase-change process. Modeling of the plume propagation in a vacuum and background gas has also been reported systematically [26]. The interaction of the plume with ambient gas significantly suppresses the void formation and phase explosion. On the other hand, no obvious effect is observed on the stress wave within the target. Interestingly, secondary stress waves resulting from redeposition of ablated atoms and void collapse are observed although their magnitude is much smaller than the direct, laser-induced stress wave [23]. The spatial confinement-induced temperature rise has been reported earlier [24]. Furthermore, the effect of scanning probe microscopy tip confinement in nanostructuring has also been studied previously [25]. The dynamics of melting a surface nanolayer and the formation of thermal and shock waves in metals irradiated by femtosecond laser pulses have been investigated both experimentally and theoretically [27]. A microexplosion in a confined domain results in the formation of a submicron cavity. Numerical simulations have shown that the cavity size is strongly dependent on the parameters of the equation of state, such as the Grüneisen coefficient or the latent heat of sublimation [28]. However, the solid-to-super critical phase change during the internal ablation confined by the target has not yet been investigated.

In this study, MD simulations are carried out to investigate picosecond laser ablation inside an argon crystal of 3,200,000 atoms. Emphasis is placed on understanding the mechanism of the phase change from a solid to a supercritical fluid during laser ablation inside the target. Laser-induced heat transfer, stress waves, phase change, and material ablation are studied. The material undergoes an extremely confined phase-change process, resulting in a maximum temperature that can exceed the thermodynamic critical point. It is always desirable to simulate a real material that is used in laser internal ablation, such as Si or SiO₂, and compare the results with experimental data for understanding the mechanism. However, for the target size ($108.28 \times 10.82 \times 108.28 \text{ nm}^3$) and time duration (1.46 ns) simulated in this study, the simulation of real materials will be orders of magnitude more time consuming. This will make the work much less feasible. Therefore, we choose argon crystal to investigate the rapid phase-change process and thermodynamic trajectories of materials during picosecond laser internal ablation. The parameters relevant to laser ablation, such as the temperature, stress, and volume in the laser ablation process, are studied in detail. The orientation–radial distribution function (ODF) provides crucial information about the atomic density and angle distribution of the crystal structure.

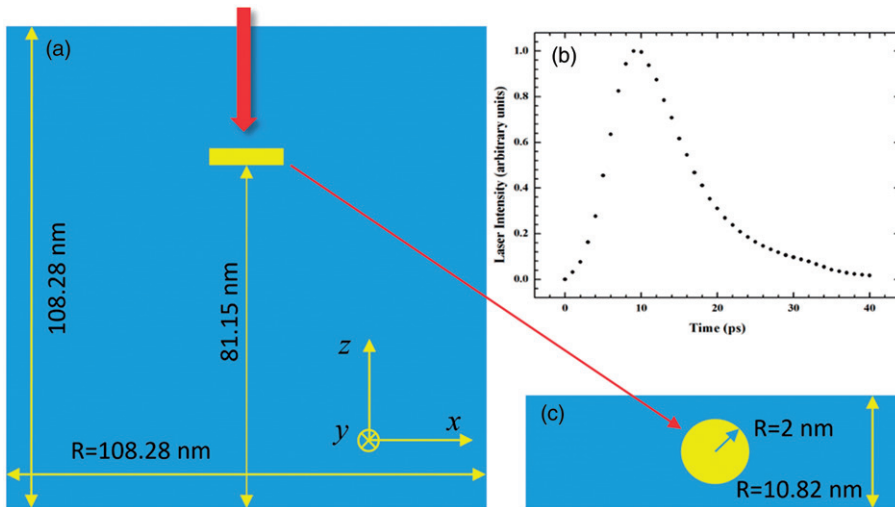


Figure 1. Physical model for simulating the laser internal ablation in nanostructuring process.

Physical domain construction and modeling

Figure 1a shows the physical model of the simulation domain structure. A circular region with $R = 2$ nm in the target at $z = 81.15$ nm is ablated by a picosecond laser. The target has dimensions of 108.28 nm \times 10.82 nm \times 108.28 nm ($x \times y \times z$). Figure 1b shows the intensity distribution of the picosecond laser. The full-width at half-maximum of the picosecond laser peaks at $t = 9$ ps. Figure 1c shows the profile of the circular region. The thickness of the simulated system in the y direction is 10.82 nm, which is relatively small compared with the thicknesses in the x - and z -directions. This quasi-2D design enables the phase change and stress waves to be studied over a very long time. Periodic boundary conditions are applied in the x - and y -directions. The boundary conditions in the z -direction are the absorptive boundary condition at the bottom and the shrink boundary condition at the top. An effective absorptive boundary condition should accurately simulate the wave radiation into the exterior while keeping the computational cost low [29–31]. A strong stress wave emerges in the material when a picosecond laser pulse irradiates the material from the top side. The stress wave then propagates to the bottom boundary of the MD domain, which results in a strong tensile stress, causing tearing in the material near the bottom boundary. The treatment using absorptive boundaries has been demonstrated to work well in eliminating reflection of the shock wave and avoiding undesired material damage in the boundary region. A 10 Å-thick region along the z -axis at the bottom of the target is chosen as the absorptive boundary. An external force specified by the earlier study [30, 32] is added to the atoms in this region. For the shrink boundary condition, the position of the face is set to encompass the atoms in that dimension (shrink wrapping) irrespective of how far they move. The upper boundary is a shrink boundary to observe the shift when the atoms move out of the surface. The stress waves are not absorbed by the shrink boundary and could influence the surface state. The interaction among atoms follows the Lennard–Jones (12-6) potential, and the laser irradiation in the simulation is focused on a circular spot with a radius of 2 nm in the target. However, actual illuminated spot sizes are at least approximately the same as the optical wavelength, which is in the order of 1 μ m. The 2 -nm radius of the disk used as the absorptive body in the presented simulations can reduce the number of simulated atoms while still revealing the mechanism of the internal ablation. A single 40 -ps laser pulse is applied in this simulation, and the laser energy is spatially uniform over the spot. The laser absorption region is divided into a number of cells with a thickness $\Delta z = 1$ nm to ensure that the laser energy absorption obeys the Beer–Lambert law. The absorption

depth is defined as 5 nm in the simulation, which is within the range of the values appropriate for absorbing molecular solids. The laser beam absorption is achieved by scaling the velocity of the atoms in the cell while keeping the momentum conserved. The incident laser energy decreases exponentially after the absorption by atoms in each cell. The details have been documented in the previously published studies [32, 33].

While at thermal equilibrium, the system is first run for 1.25 ns under a 50 K canonical ensemble (NVT) condition and then run under a microcanonical ensemble (NVE) condition for 500 ps. Different laser energies are tried for the modeling. A cavity is finally formed when the laser energy is $E = 13 \text{ J/m}^2$, and material is ejected during laser heating when the laser energy is $E = 15 \text{ J/m}^2$. Therefore, the laser energy of $E = 10 \text{ J/m}^2$ is chosen for the simulation, and the system is run under NVE conditions for recrystallization with a 2-fs time step during laser ablation. For the MD simulations, because of the limited computing power, the number of atoms in the system has been restricted. To facilitate the simulation, the system that contains a large number of argon atoms (3,200,000 atoms) with a cubic structure is selected as the material. This system is easy to model and enables rapid computation while the conclusion does not lose its generality. The validity of this approach has been demonstrated in the laser-material interaction simulations of earlier studies [23, 32–36]. The laser absorption process depends on the laser wavelength and the light absorption characteristics of the material. The Lennard–Jones potential well depth ε is chosen as 0.0103 eV, the equilibrium separation parameter σ is 3.406 Å, and the cutoff distance is set to 2.5σ . At this distance, the potential is only approximately 1.6% of the well depth. The atomic distance is compared with r_c using the cell structure and linked list method [37]. Unlike classical continuum modeling, MD simulations do not need mechanical and thermal properties input and their dependence on temperature and pressure. The system itself directly simulates the movement of atoms. The macroscale properties of the system such as temperature, stress/pressure, and crystalline structure are directly evaluated based on the microscale properties of atoms (e.g., potential, velocity, and position). Large-scale Atomic/Molecular Massively Parallel Simulator (LAMMPS) is used for the simulations in this study [38]. Even there are large number of atoms, the scale of the target is very small, and hence Å (10^{-10} m) and nm (10^{-9} m) are chosen for the unit of the scale. The pressure of target irradiated by laser is very high, and hence bar (10^5 Pa) is chosen for the unit of the pressure.

Phase change and stress-induced structure damages

The incident laser and target material properties strongly affect the internal nanostructures. The case with a laser fluence is $E = 10 \text{ J/m}^2$ is chosen to obtain the general picture of the laser ablation, stress wave generation and propagation, and recrystallization processes. Figure 2 shows the atomic snapshots at different times of this case as the laser energy is applied from 0 to 40 ps. The ablation clearly starts 5 ps. The dark area in the target indicates the destruction of the crystal. Some destruction is permanent because the destruction region even shrinks at the final state compared with the initial moment after the laser pulse. No voids are observed within the material during our modeling time.

The thermal expansion duration of material is quite long-time process relative to the very short duration of the laser pulse. The figures from $t = 5$ to $t = 100$ ps show the thermal expansion and relaxation of the target. The pictures from $t = 200$ to $t = 1460$ ps show the recrystallization of the target. The well-arranged crystal structure of the material is distorted by the strong stress wave in the target. These can be clearly observed in the snapshots at 50, 100, and 200 ps as large and irregular gray areas emerge surrounding the laser heating region. This is because when the crystalline structure is distorted, the atomic position becomes very irregular, and the area becomes gray. The changes in the atomic configuration show that much of the temporary damages/structure distortion could return to the well crystalline structure after the stress wave passes

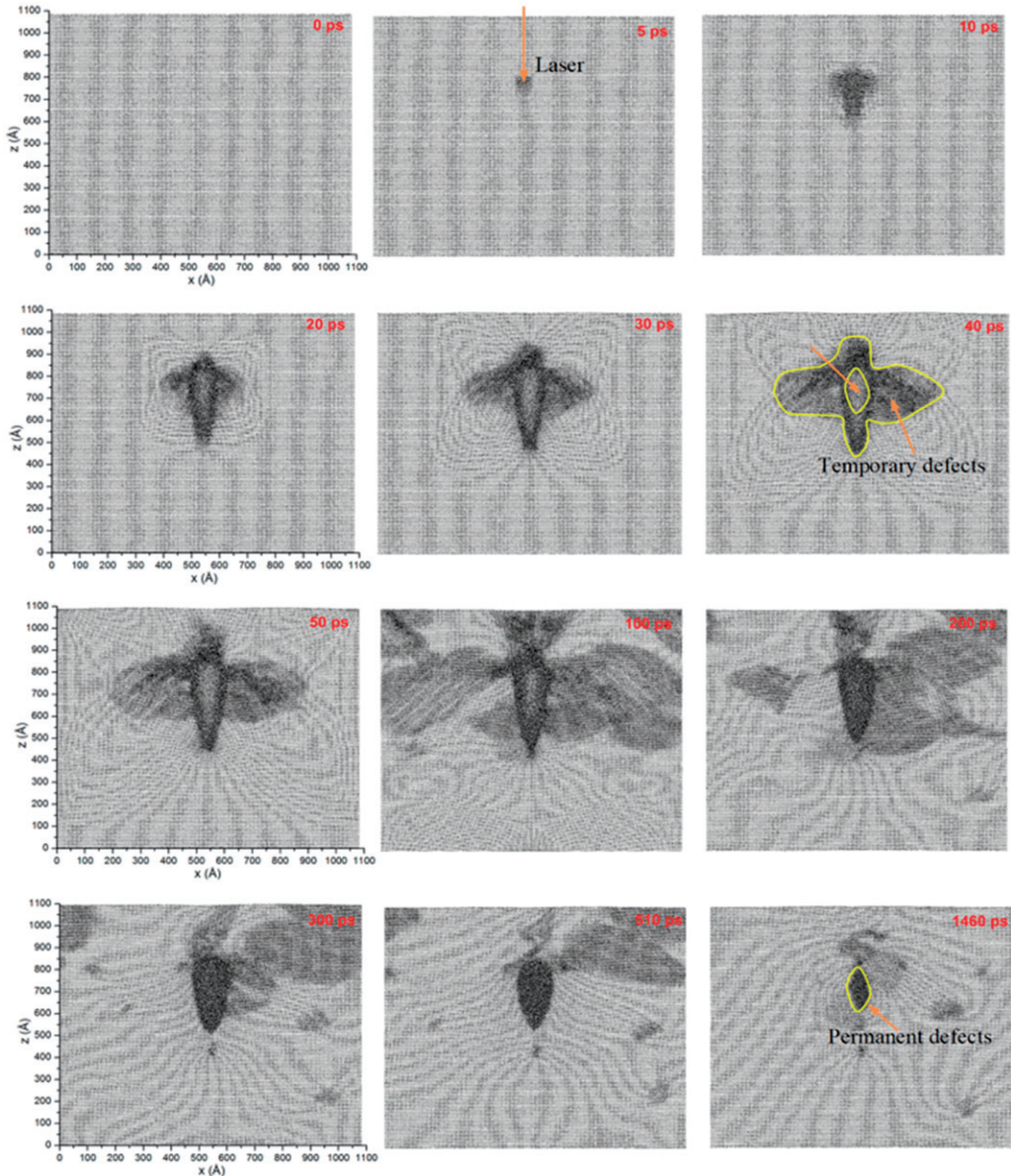


Figure 2. The snapshots of atomic positions to show the structure evolution induced by stress wave.

that region. The change of the structure damaged area (gray cloud) varies in space from 50 to 510 ps, reflects and is correlated with the stress wave propagation in space. However, some destruction is permanent. At the end of the simulation ($t = 1460$ ps), defects in the target (pretty much the initial laser beam absorption region) are still observed and almost no damage recoveries are observed over the last 50 ps of the simulation.

Figure 3 shows the stress contour of the system. In the beginning of laser heating, the stress wave generation and propagation experiences very large magnitude change. The stress refers to the internal forces that neighboring particles in a continuous material exert on each other and is calculated as $\sigma = (\sigma_{xx} + \sigma_{yy} + \sigma_{zz})/3$ for our result's discussion. Hence, we do not distinguish the normal stress in different directions although there should be some difference among them.

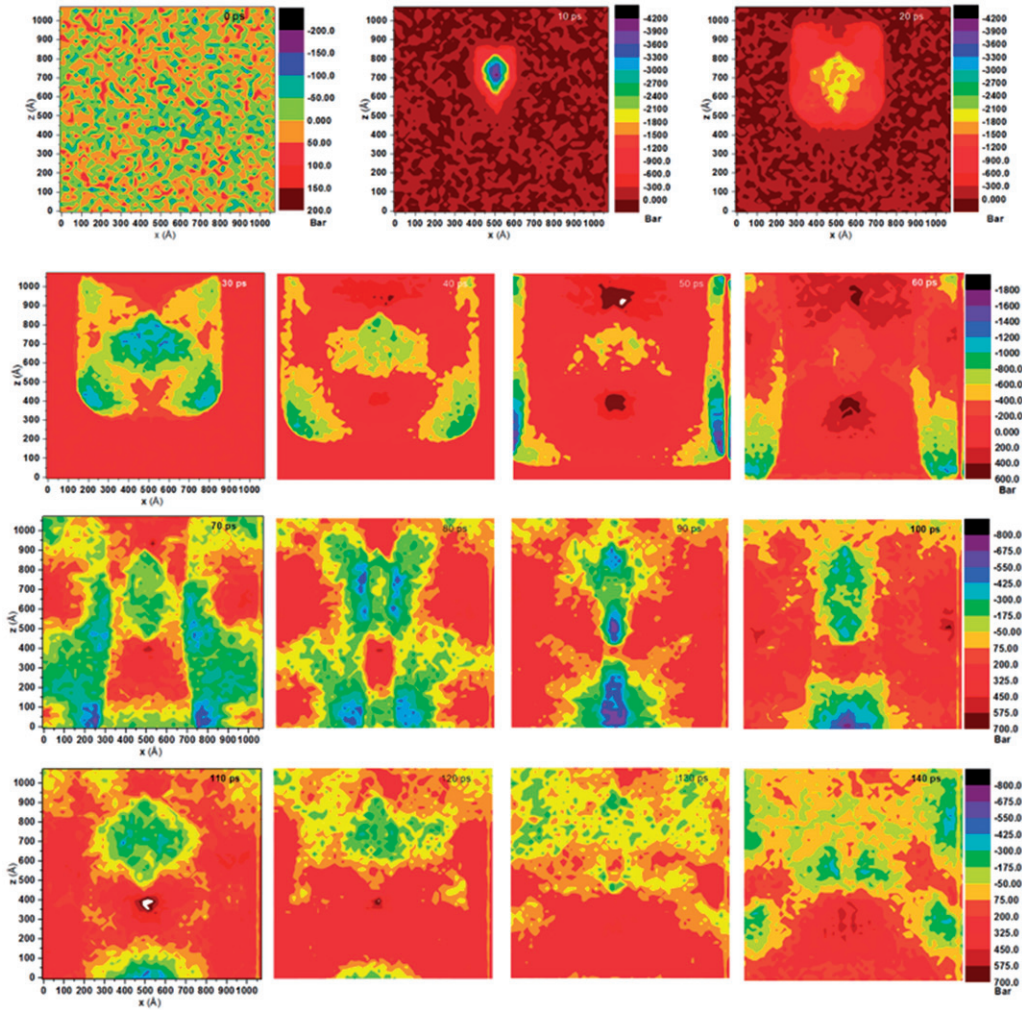


Figure 3. Stress contours at different times of the process to illustrate the development and propagation of the stress wave.

Detailed analysis and discussion of all the stress components (normal and shear stress) and their generation and propagation in space can be found in the study by Wang [39]. To view the intense stress change in the beginning of laser heating, we have to use different magnitude scales. These are shown in the first three figures at 0, 10, and 20 ps. A large compressive stress emerges inside the solid at the beginning of laser ablation. With the phase change and shock wave propagation, the pressure periodically changes and decreases gradually (30–260 ps). At approximately $t = 50$ ps, the stress wave reaches the x -boundary and re-enters the domain from the other side because of the periodical boundary conditions. Then, the stress waves converge in the center of the x -direction at $90 \leq t \leq 100$ ps, and the pressure decreases at 100 ps. This periodic stress wave propagation has a period of approximately 80 ps, and the stress wave in the target is very clear. Our previous study has presented a detailed analysis and discussion of the stress wave in a solid [34, 40] under laser ablation. The stress wave forms at 10 ps and propagates in the x - and z -directions. The stress moves from the center to the boundary at the beginning of the process. Before $t = 50$ ps, the spreading of the stress wave from the center is observed. The stress wave re-enters from the opposite side to the center at approximately $90 \leq t \leq 100$ ps, which is obvious in the x -direction because of the periodic boundary conditions. The re-entered stress wave appears at

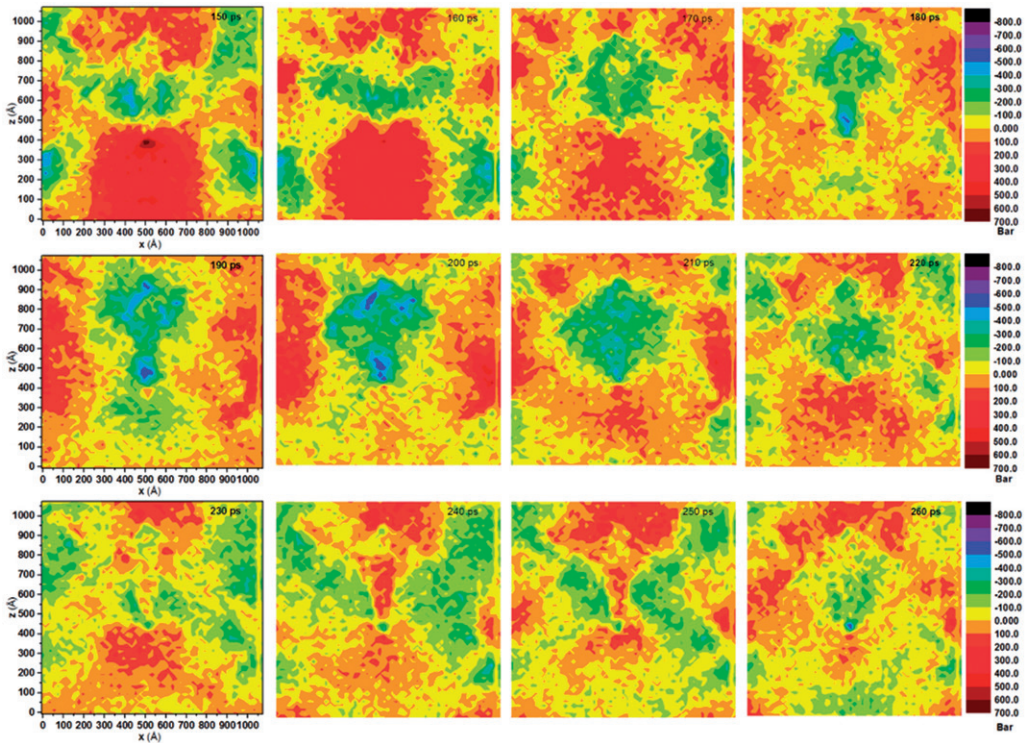


Figure 3. (Continued)

approximately $t = 180$ ps and again at $t = 260$ ps. This result reflects the periodic process of stress wave propagation with a period of approximately 80 ps, as it is also shown in Figure 4. Based on this time duration, the stress wave speed is calculated as 1354 m/s, very close to the local speed of sound (1275 m/s) in argon [41].

Figure 5 shows the temperature contours at various instances. The nonuniform temperature distribution and its extremely large gradient is the driving force of the stress wave generation. The laser starts to irradiate the target at $t = 0$ ps when the entire system is in a thermodynamic equilibrium state at $T = 50$ K. Upon laser irradiation, the temperature of the target region under direct laser irradiation rises rapidly. From $t = 10$ to $t = 40$ ps, the high-temperature region expands as a result of heat conduction between the heating region and its surroundings, which results in ablation. The regional temperature then falls during the recrystallization process, as observed from 40 to 1460 ps. The highest temperature of the target decreases to 102 K at $t = 220$ ps, 87 K at $t = 440$ ps, and 68 K at $t = 1460$ ps. The melting temperature of crystalline argon under normal conditions is 83.95 K. The cooling to near the initial temperatures and the crystallization are the results of the internal energy transfer from the hot spot by heat conduction. At the end of the simulation at $t = 1460$ ps, the regional temperature decreases to approximately 60 K. The temperature fluctuates corresponding to the stress wave. The temperature decreases as heat conduction occurs but increases slightly when the stress wave (compressive stress) begins to re-enter. A small region of $20 \text{ nm} \times 20 \text{ nm}$ ($x \times z$) in the laser irradiated region is chosen to explain this fluctuation. The center coordinate of this small region is $(552.8, 752.8)$ (x, z).

Figure 4 shows the temperature and stress of this small region at different times. An interesting phenomenon in Figure 4 is that the temperature increases from 80 to 110 ps and from 150 to 180 ps although the overall tendency of the temperature is decreasing. The conduction cooling is the main mechanism of the temperature decrease. The small fluctuations in temperature mean

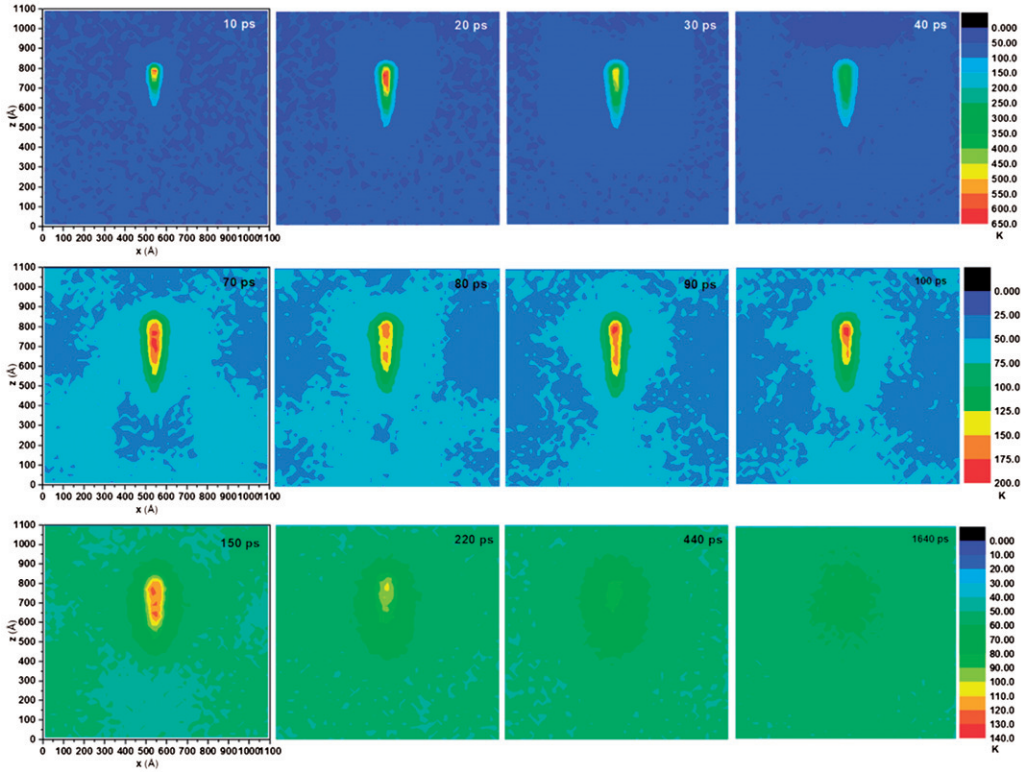


Figure 4. Temperature and stress of the small region at different times.

that acoustic heating also affects the temperature, but to a much lower degree than the conductive cooling. The fluctuation in the temperature is owing to the heating and cooling by the compression and rarefaction waves. The effect on the local temperature change induced by the coupling between the temperature and the strain rate is proportional to the local strain rate. These results confirm the analytical solutions drawn by Wang and Xu [34] that the relationship between temperature and stress is given as

$$\frac{\partial T}{\partial t} = -\frac{B\beta_T T_0}{(B + 4/3G)\rho c_p} \frac{\partial \sigma}{\partial t} \tag{1}$$

where B is the bulk modulus, G is the shear modulus, σ the stress, the bulk modulus, β_T volumetric thermal expansion coefficient, and ρ the density.

Phase-change characteristics

Figure 6a shows the thermodynamic analysis of atomic groups under a laser energy fluence of 10 J/m^2 at 1460 ps. As shown in Figure 6b, all groups have returned to the solid phase at 1460 ps and remain there. Their thermodynamic trajectories of pressure and temperature during the ablation process are shown in Figure 6b in which the arrows indicate the progress of time. The phase boundary lines between the solid, liquid, and gas phases are taken from the standard argon diagrams. The black solid line is the phase boundary between liquid and gas; the red solid line is the phase boundary between solid and liquid. The material phase changes of groups 1, 2, 3, and 4 are shown in Figure 6b. The pressure of the groups suddenly increases over the critical pressure. Groups 1, 2, 3, and 4 change from solids to liquids; group 4 then returns directly to the solid phase, whereas groups 1, 2, and 3 turn into supercritical fluids and finally back into solids. In

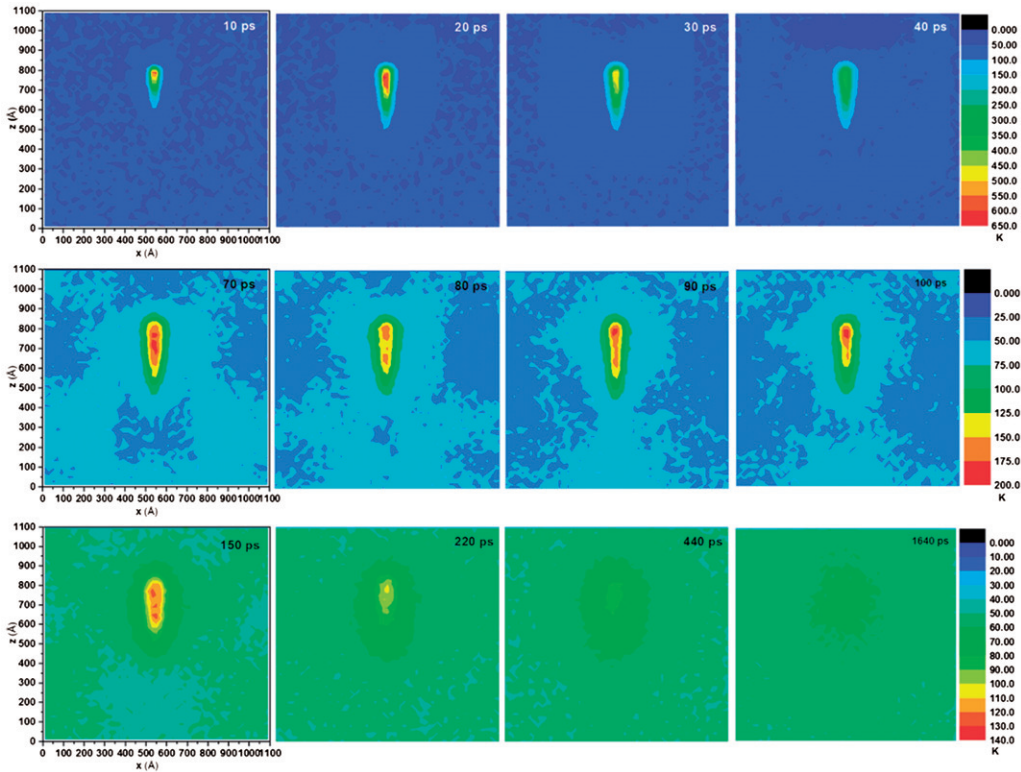


Figure 5. Temperature contours at different times to illustrate the heating, cooling, and stress wave-induced temperature change.

contrast, group 5, which does not contact the solid–liquid phase boundary, does not undergo a phase change. When the laser irradiates the surface of the target, some groups of the material are first increased to a temperature higher than the critical temperature and become a supercritical fluid [4]. After expansion, their temperatures decrease and they enter the unstable zone below the critical point as phase separation occurs. When the laser irradiates the interior of the target as studied in this article, the thermodynamic trajectories of the groups suggest that the material can

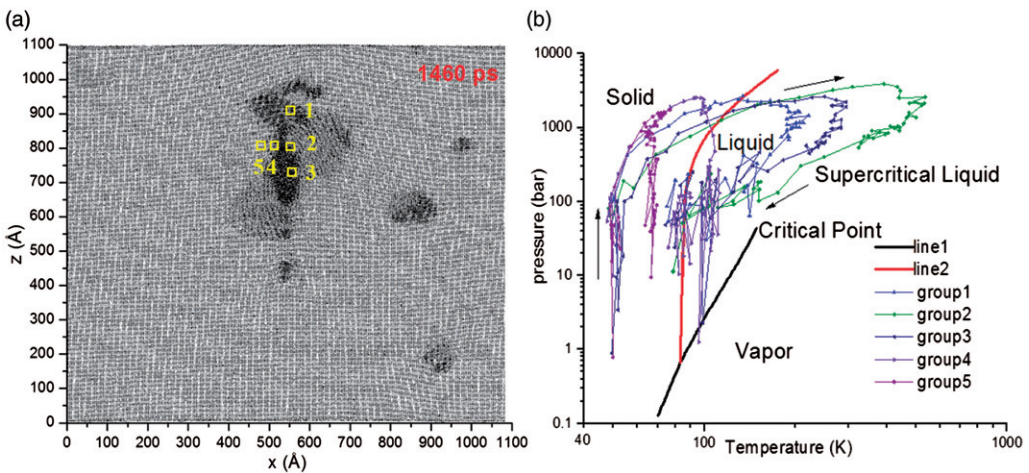


Figure 6. Thermodynamic trajectories of the atoms groups during laser internal ablation in the P - T diagram.

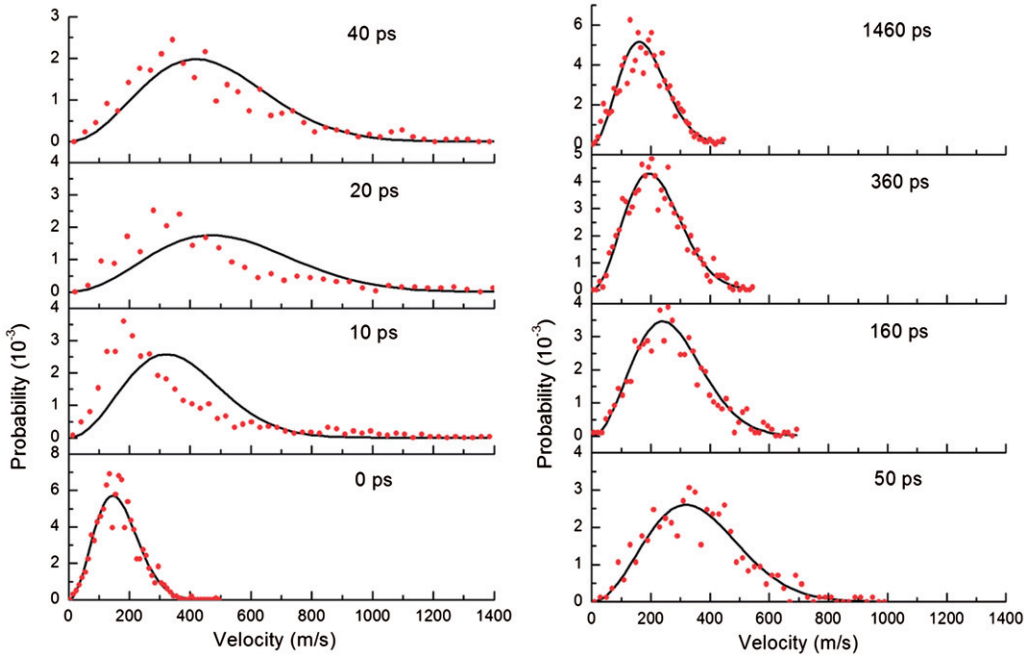


Figure 7. Velocity distributions (red dots) compared with Maxwellian distribution (black line) for group 2 in Figure 6a.

turn into a supercritical fluid and then return to a solid under the laser fluence, which is very different from the laser ablation of the target surface.

In the previous discussion, the overall temperature is defined when the system achieves local thermal equilibrium, which can be verified by studying the velocity distribution at the location of interest and comparing it to the Maxwell–Boltzmann distribution. Figure 7 shows the Maxwell–Boltzmann distributions and the velocity distributions of the atoms in group 2 are shown in Figure 6a. The solid line is the Maxwellian distribution, and the red dots are the MD simulation results. The atomic velocity before the laser radiation is observed to closely follow the equilibrium Maxwell–Boltzmann distribution. During the 40 ps of laser heating, the thermal equilibrium cannot be fully established. After this point, however, the atomic velocity again follows the equilibrium Maxwell–Boltzmann distribution. The Maxwellian distribution is fitted using both the temperature and the velocity to subtract the effects of the macroscopic velocity.

In this internal ablation, the entire process occurs within an extremely confined domain. An interesting question is: Whether the phase state still follows that of normal argon. This study is conducted and summarized for group 2 in Table 1. In Table 1, T_1 is the temperature of normal argon defined by the pressure P and specific volume ν , which is given by the MD results, and T

Table 1. Comparison of the temperature T_1 which is calculated by state software using parameters P and ν and T which is calculated by MD.

Time (ps)	P (MPa)	ν ($10^6 \text{ m}^3/\text{mol}$)	T_1 (K)	T (K)
10	322.7	25.79	197	266
20	199.3	43.89	539	521
30	101.3	55.48	455	440
40	53.5	55.71	303	322
60	30.4	53.98	224	208
160	15.9	37.95	149	135
360	30.2	29.90	115	96
440	8.6	29.87	102	82

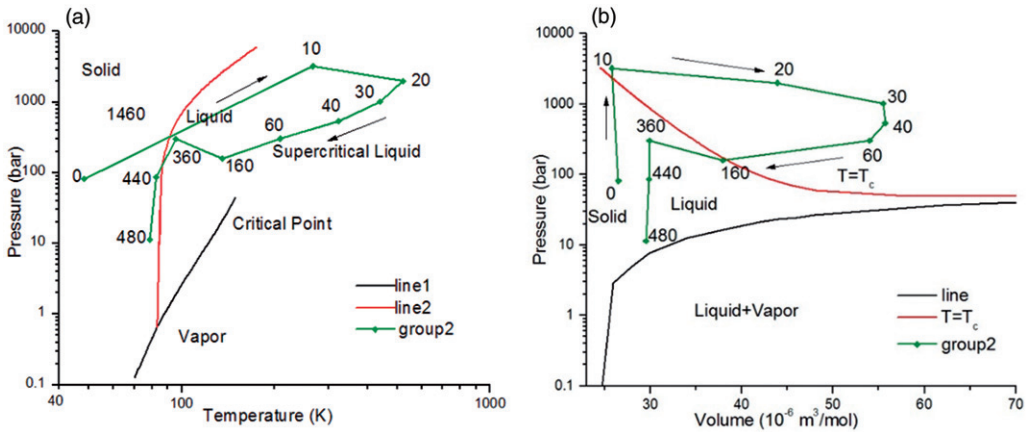


Figure 8. Thermodynamic trajectories of the atoms groups at laser internal ablation in the P - T (a) and P - v diagram (b).

is calculated with LAMMPS in the MD simulation. The results indicate that the status of the argon calculated by MD is approximately consistent with the parameters of the macroscopic status points.

Interestingly, as shown in the last line of Table 1, at $t = 440$ ps, from Figure 8, the P - T and P - v diagrams at a number of time steps show that the argon is solid near the solid-liquid separation line. This behavior does not follow the status of normal argon. When the P - v diagram is used to show the status of argon, the boundary line between solid and solid-liquid is approximated by the line of $v = 24.72 \text{ m}^3/\text{mol}$, which can be calculated from the density of solid argon. In the initial state, the specific volume of the entire target is $23.89 \text{ m}^3/\text{mol}$, calculated by the lattice constant of 0.5414 nm and 4 atoms per atomic cell. At the beginning of the laser radiation, the specific volume of group 2 is approximately $26 \text{ m}^3/\text{mol}$, which is greater than the nominal value. The discrepancy arises because the selected area is $2 \times 2 \text{ nm}$ but the lattice constant is 0.5414 nm ; thus, some atoms may not be included in the group, which makes the calculated value of the specific volume higher than the actual specific volume. As shown in Figure 8, the status point of 440 ps is near the solid-liquid boundary but in solid region of the P - T diagram. Given the discrepancy owing to the chosen small region, the actual specific volume is lower than the calculated volume by approximately $2\text{--}3 \text{ m}^3/\text{mol}$. The phase of the 440 ps point on the P - v diagram is also in the solid region, which matches the phase point on the P - T diagram. This observation also explains the discrepancy between T and T_1 in Table 1.

Crystallinity and ODF

Alternative parameters for looking into the material structure have been proposed, including the local order parameter [42] and the centrosymmetry parameter [43, 44]. In this study, crystallinity is used to study the material state at the atomic level. This approach is designed to reveal whether the material is close to a perfect crystalline state. The crystallinity function is defined as follows [35]

$$\phi(r_{i,x}) = \frac{1}{N} \left| \sum_i e^{j2\pi(2r_{i,x}/\lambda)} \right| \quad (2)$$

where $r_{i,x}$ is the x coordinate of atom i , N is the number of atoms, and λ is the light wavelength for crystallinity characterization assigned with the lattice constant of $b = 5.414 \text{ \AA}$. If the atoms are regularly distributed in space with their spacing in the x -direction equal to $n(b/2)$, the function will be equal to 1. If the material is in an amorphous state, the function will be much < 1 .

Figure 9 shows the contour of how the crystallinity changes with time. The entire region is divided into cubes of dimensions $1 \times 10.82 \times 1$ ($x \times y \times z$) nm³. Some representative time points are chosen to illustrate the change in the structure. The crystallinity's value reflects the structure of the material: values close to 1 indicate a crystal structure close to the original state at $t = 0$ ps, and low values indicate an amorphous state. The structure adjacent to the melting region is also destroyed as shown over the entire process. In the recrystallization process, permanent defects can be observed in the laser irradiation spot and are characterized by the low crystallinity value at $t = 1460$ ps. Compared with the stress distribution graph, the crystallinity decreases drastically when the stress wave passes through, which is shown by the various light-blue cloud regions at 30–1460 ps. This indicates the structure change resulting from the high compressive stress. Such structure change is mostly temporary. At 10 ps, the atoms in the irradiation zone experience a sudden temperature increase because of the high laser fluence. The stress wave travels in the materials and reaches the center again at $t = 150$ ps, which decreases the crystallinity at that moment. After the stress wave passes and dissipates, the crystallinity of the damaged zone increases slowly to 1, which indicates that part of the material recrystallizes after the ablation (Figure 9) corresponding to 1460 ps.

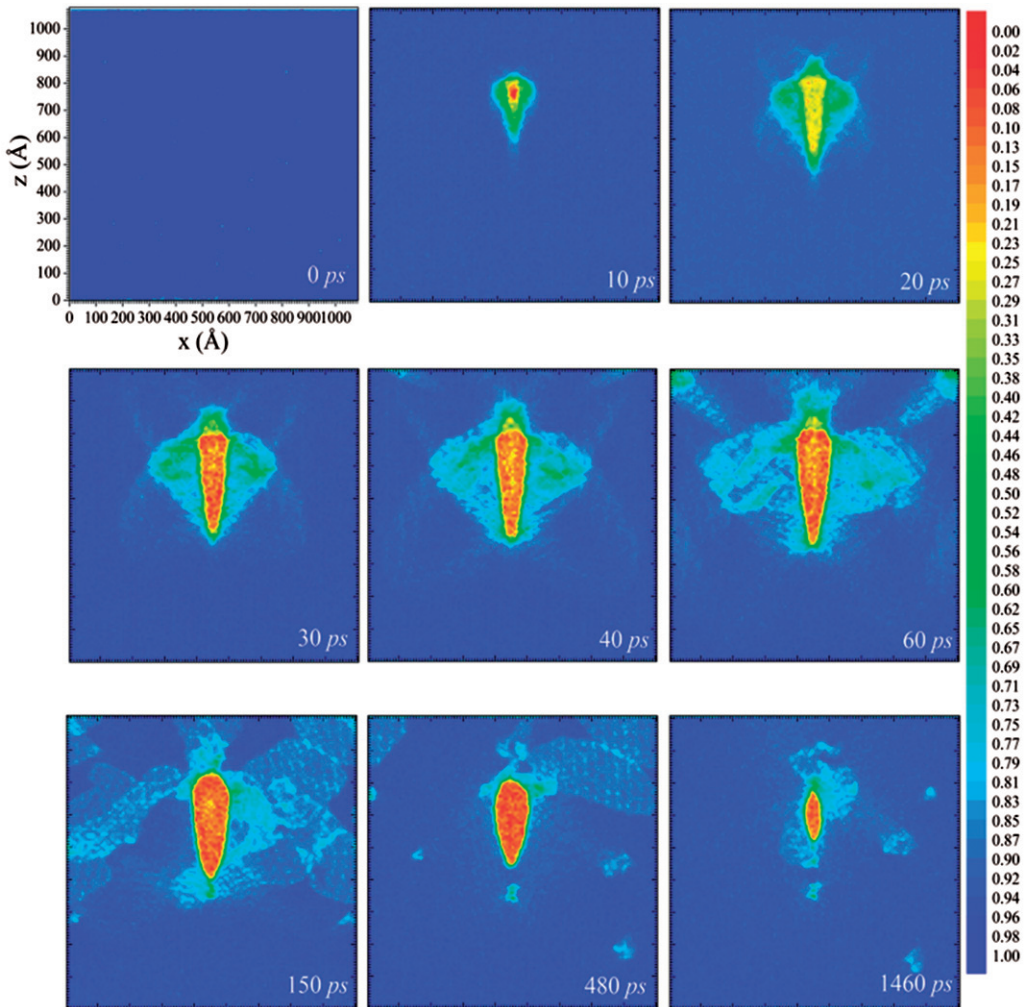


Figure 9. Crystallinity contours at different times to show the phase-change process.

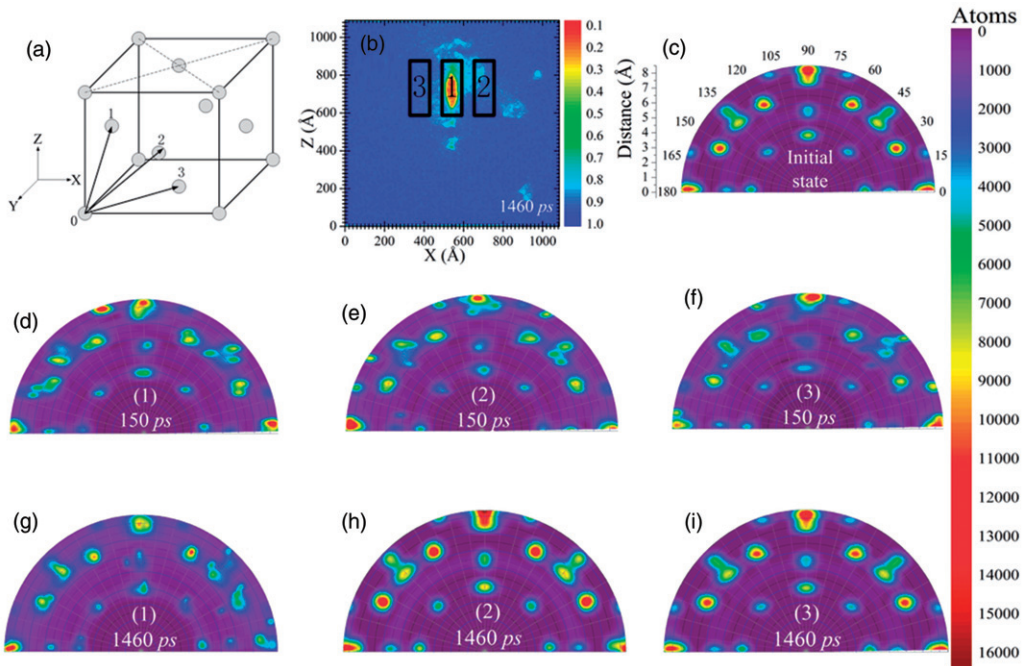


Figure 10. Polar contours of the ODF of different regions at 150 and 1460 ps.

Although the destruction of the crystal structure is well illustrated by the crystallinity function, the question of whether the crystal is partially amorphous or just twisted orientationally remains unanswered. Under the influence of the stress wave during the ablation process, material structures could be easily twisted, changing the crystallographic orientation. This change makes the final spatial structure of the crystal substantially different from the initial crystallographic orientation. The ODF has been developed to study this problem [35]. The ODF provides information about the atomic density and angular distribution of the crystal structure.

The 3D image of the face-centered cubic (FCC) structure of the argon crystal is shown in Figure 10a. As evident in the graph, atoms 1, 2, and 3 are those nearest the origin. In this study, the atomic distance is calculated from 3D space and the angle is obtained from all the atoms projected onto the X - Y plane. At the initial state, the nearest atoms are at 0 , $\pi/4$, $\pi/2$, $3\pi/4$, and π in the ideal situation.

Some defects remain after the cooling process as shown in Figure 9. Three regions as shown in Figure 10b are chosen to illustrate the relationship of the ODF to the observed defects. Region 1 is the permanent defect and regions 2 and 3 are the areas near region 1. The volumes of the three areas are the same; thus, they initially have approximately the same number of atoms (approximately, $58,530 \pm 20$). The atoms are all perfectly located in their positions according to FCC structure at the initial state as shown in Figure 10c. The ODF includes information about the atomic density variation in different angles. Before the laser energy is applied to the materials, the ODF of the crystal is exactly symmetric, which indicates that the structure of the crystal, which is free of defects, includes a large number of atoms distributed at certain radii (4.275, 6.525, and 8.325 Å). After the laser energy is applied to the material, the atoms are twisted to other angles, as shown in the ODF at 150 ps. In contrast to the temperature distribution, the atoms are relocated to their proper positions during the cooling process, and hence introducing partial defects that must be repaired. Figure 10d,g show that the angles of a large number of atoms in region 1 are twisted and badly disorganized at 150 and 1460 ps. In contrast, regions 2 and 3 contain only slight defects. As shown in Figure 10e,h,f,i, the atoms in these two regions are

located almost perfectly around the specific angles at 1460 ps. This observation illustrates well that the target will be in the solid phase at the end of the process. However, twisted atoms that result in permanent defects are still present.

Conclusion

In this study, systematic atomistic modeling was conducted to elucidate the phase change, stress wave generation, propagation, and the resulting structure damage (temporary and permanent) during picosecond internal laser ablation. Under the investigated conditions, the material destruction in the internal laser-irradiated region may become permanent. At the end of the simulation at $t = 1460$ ps, defects were still observed in the target. The propagation of stress waves and fluctuations of the temperature during the recrystallization process were periodic and highly correlated. The initial peak temperature inside the target exceeds the critical temperature, which makes the solid argon change to a supercritical fluid. However, the supercritical–fluid argon returned to the solid phase because of the space constraint imposed by the stress and space. This is very different from the ablation of the material surface by the similar laser. The ODF well illustrated that the permanent defect is owing to atom twisting. Further analysis of the simulation results to clarify the role of the laser radiation and atomic interaction in the form of permanent defects would be informative.

Disclosure statement

No potential conflict of interest was reported by the author(s).

Funding

Support of this work was by the National Science Foundation of China (No. 51376164), the Key Research and Development Program of Shandong Province (No. 2017GHY15113) and China Scholarship Council (No. 201406335016).

ORCID

Xinwei Wang  <http://orcid.org/0000-0002-9373-3750>

References

- [1] B. N. Chichkov, C. Momma, S. Nolte, F. von Alvensleben, A. Tünnermann, “Femtosecond, picosecond and nanosecond laser ablation of solids,” *Appl. Phys. A*, vol. 63, no. 2, pp. 109–115, 1996. DOI: [10.1007/BF01567637](https://doi.org/10.1007/BF01567637).
- [2] M. Stafé, C. Negutu, N. N. Puscas, “Pulsed laser ablation of solids,” *Rom. Rep. Phys.*, vol. 62, pp. 758–770, 2010.
- [3] S. Backus, C. G. Durfee III, M. M. Murnane, H. C. Kapteyn, “High power ultrafast lasers,” *Rev. Sci. Inst.*, vol. 69, no. 3, pp. 1207–1223, 1998. DOI: [10.1063/1.1148795](https://doi.org/10.1063/1.1148795).
- [4] C. Cheng and X. Xu, “Mechanisms of decomposition of metal during femtosecond laser ablation,” *Phys. Rev. B*, vol. 72, no. 16, pp. 165415, 2005. DOI: [10.1103/PhysRevB.72.165415](https://doi.org/10.1103/PhysRevB.72.165415).
- [5] L. V. Zhigilei, Z. Lin, and D. S. Ivanov, “Atomistic modeling of short pulse laser ablation of metals: Connections between melting, spallation, and phaser explosion,” *J. Phys. Chem. C*, vol. 113, no. 27, pp. 11892, 2009. DOI: [10.1021/jp902294m](https://doi.org/10.1021/jp902294m).
- [6] R. Kelly and A. Miotello, “Comments on explosive mechanisms of laser sputtering,” *Appl. Surf. Sci.*, vol. 96–98, pp. 205–215, 1996. DOI: [10.1016/0169-4332\(95\)00481-5](https://doi.org/10.1016/0169-4332(95)00481-5).
- [7] K. H. Song and X. Xu, “Explosive phase transformation in excimer laser ablation,” *Appl. Surf. Sci.*, vol. 127–129, pp. 111–116, 1998. DOI: [10.1016/S0169-4332\(97\)00619-3](https://doi.org/10.1016/S0169-4332(97)00619-3).

- [8] V. P. Skripov and A. V. Skripov, "Spinodal decomposition (phase transitions via unstable states)," *Soviet Phys. Uspekhi*, vol. 22, no. 6, pp. 389–410, 1979. DOI: [10.1070/PU1979v022n06ABEH005571](https://doi.org/10.1070/PU1979v022n06ABEH005571).
- [9] V. V. Zhakhovskii, K. Nishihara, S. I. Anisimov, and N. A. Inogamov, "Molecular-dynamics simulation of rarefaction waves in media that can undergo phase transitions," *JETP Lett.*, vol. 71, no. 4, pp. 167–172, 2000. DOI: [10.1134/1.568306](https://doi.org/10.1134/1.568306).
- [10] M. E. Povarnitsyn, T. E. Itina M. Sentis, and P. R. Levashov, "Material decomposition mechanisms in femtosecond laser interactions with metals" *Phys. Rev. B.*, vol. 75, 235414 2007. DOI: [10.1103/PhysRevB.75.235414](https://doi.org/10.1103/PhysRevB.75.235414).
- [11] X. Xu and D. A. Willis, "Non-equilibrium phase change in metal induced by nanosecond pulsed laser irradiation," *J. Heat Transfer.*, vol. 124, no. 2, pp. 293–298, 2002. DOI: [10.1115/1.1445792](https://doi.org/10.1115/1.1445792).
- [12] X. Xu, "Heat transfer and phase change during high power pulsed laser ablation of metal," *Annual Rev. Heat Transfer.*, vol. 12, no. 12, pp. 79–115, 2002. DOI: [10.1615/AnnualRevHeatTransfer.v12.50](https://doi.org/10.1615/AnnualRevHeatTransfer.v12.50).
- [13] P. Lorazo, L. J. Lewis, and M. Meunier, "Thermodynamic pathways to melting, ablation, and solidification in absorbing solids under pulsed laser irradiation," *Phys. Rev. B*, vol. 73, no. 13, pp. 134108, 2006.
- [14] X. Xu, C. Cheng, and I. H. Chowdhury, "Molecular dynamics study of phase change mechanisms during femtosecond laser ablation," *J. Heat Transfer.*, vol. 126, no. 5, pp. 727–734, 2004. DOI: [10.1115/1.1797011](https://doi.org/10.1115/1.1797011).
- [15] M. Masuda *et al.*, "3-D microstructuring inside photosensitive glass by femtosecond laser excitation," *Appl. Phys. A*, vol. 76, no. 5, pp. 857–860, 2003. DOI: [10.1007/s00339-002-1937-z](https://doi.org/10.1007/s00339-002-1937-z).
- [16] M. Kim, D. J. Hwang, H. Jeon, K. Hiromatsu, and C. P. Grigoropoulos, "Single cell detection using a glass-based optofluidic device fabricated by femtosecond laser pulses," *Lab Chip*, vol. 9, no. 2, pp. 311–318, 2009. DOI: [10.1039/B808366E](https://doi.org/10.1039/B808366E).
- [17] R. Taylor, C. Hnatovsky, and E. Simova, "Applications of femtosecond laser induced self-organized planar nanocracks inside fused silica glass," *Laser Photon*, vol. 2, no. 1–2, pp. 26–46, 2008. DOI: [10.1002/lpor.200710031](https://doi.org/10.1002/lpor.200710031).
- [18] Y. Shin, S. Park, Y. Kim, and J. S. KNelson, "Analysis of laser engraving image inside crystal and PMMA," *Proc. SPIE*, vol. 5713, pp. 539–544, 2005. DOI: [10.1117/12.590773](https://doi.org/10.1117/12.590773).
- [19] T. Kim, S. Park, H. Oh, and Y. Shin, "Analysis of the laser patterning inside light guide panel," *Optics Laser Technol.*, vol. 39, no. 7, pp. 1437–1442, 2007. DOI: [10.1016/j.optlastec.2006.10.002](https://doi.org/10.1016/j.optlastec.2006.10.002).
- [20] B. Rethfeld, "Free-electron generation in laser-irradiated dielectrics," *Contrib. Plasma*, vol. 47, no. 4–5, pp. 360–367, 2007. DOI: [10.1002/ctpp.200710048](https://doi.org/10.1002/ctpp.200710048).
- [21] F. Quéré *et al.*, "Ultrafast carrier dynamics in laser-excited materials: Subpicosecond optical studies," *Appl. Phys. B*, vol. 68, no. 3, pp. 459–463, 1999.
- [22] N. M. Bulgakova, M. Nadezhda, V. P. Zhukov, and Y. P. Meshcheryakov, "Modification of transparent materials with ultrashort laser pulses: What is energetically and mechanically meaningful?," *J. Appl. Phys.*, vol. 118, no. 3, pp. 233108, 2015. DOI: [10.1063/1.49378964](https://doi.org/10.1063/1.49378964).
- [23] C. Li, J. Zhang, and X. Wang, "Phase change and stress wave in picosecond laser–material interaction with shock wave formation," *Appl. Phys. A*, vol. 112, no. 3, pp. 677–687, 2013. DOI: [10.1007/s00339-013-7770-8](https://doi.org/10.1007/s00339-013-7770-8).
- [24] C. Li, J. Wang, and X. Wang, "Shock wave confinement-induced plume temperature increase in laser-induced breakdown spectroscopy," *Phys. Lett. A*, vol. 378, no. 45, pp. 3319–3325, 2014. DOI: [10.1016/j.physleta.2014.06.049](https://doi.org/10.1016/j.physleta.2014.06.049).
- [25] C. Li, L. Zhang, Y. Li, and X. Wang, "Material behavior under extreme domain constraint in laser-assisted surface nanostructuring," *Phys. Lett. A*, vol. 380, no. 5–6, pp. 753–763, 2016. DOI: [10.1016/j.physleta.2015.12.001](https://doi.org/10.1016/j.physleta.2015.12.001).
- [26] L. V. Zhigilei, "Dynamics of the plume formation and parameters of the ejected clusters in short-pulse laser ablation," *Appl. Phys. A*, vol. 76, no. 3, pp. 339–350, 2003. DOI: [10.1007/s00339-002-1818-5](https://doi.org/10.1007/s00339-002-1818-5).
- [27] M. B. Agranat *et al.*, "Strength properties of an aluminum melt at extremely high tension rates under the action of femtosecond laser pulses," *JETP Lett*, vol. 91, no. 9, pp. 471–477, 2010. DOI: [10.1134/S0021364010090080](https://doi.org/10.1134/S0021364010090080).
- [28] L. Hallo, A. Bourgeade, C. Mézel, and G. Travaillé, "Formation of nanocavities in dielectrics: Influence of equation of state," *Appl. Phys. A*, vol. 92, no. 4, pp. 837–841, 2008. DOI: [10.1007/s00339-008-4580-5](https://doi.org/10.1007/s00339-008-4580-5).
- [29] L. Zhang and X. Wang, "Hybrid atomistic-macroscale modeling of long-time phase change in nanosecond laser–material interaction," *Appl. Surf. Sci.*, vol. 255, no. 5, pp. 3097–3103, 2008. DOI: [10.1016/j.apsusc.2008.08.098](https://doi.org/10.1016/j.apsusc.2008.08.098).
- [30] M. A. Zahid and M. N. Guddati, "Padded continued fraction absorbing boundary conditions for dispersive waves," *Comput. Methods Appl. Mech. Eng.*, vol. 195, no. 29–32, pp. 3797–3819, 2006. DOI: [10.1016/j.cma.2005.01.023](https://doi.org/10.1016/j.cma.2005.01.023).
- [31] V. Zhigilei and B. J. Garrison, "Pressure waves in microscopic simulations of laser ablation leonid," *MRS Proc.*, vol. 538, pp. 491–496, 1998. DOI: [10.1557/PROC-538-491](https://doi.org/10.1557/PROC-538-491).
- [32] S. Gacek and X. Wang, "Dynamics evolution of shock waves in laser–material interaction," *Appl. Phys. A*, vol. 94, no. 3, pp. 675–690, 2009. DOI: [10.1007/s00339-008-4958-4](https://doi.org/10.1007/s00339-008-4958-4).

- [33] X. Feng and X. Wang, "Effects of laser fluence on near-field surface nanostructuring," *Appl. Surf. Sci.*, vol. 254, no. 13, pp. 4201–4210, 2008. DOI: [10.1016/j.apsusc.2008.01.016](https://doi.org/10.1016/j.apsusc.2008.01.016).
- [34] X. Wang and X. Xu, "Molecular dynamics simulation of thermal and thermomechanical phenomena in picosecond laser material interaction," *Int. J. Heat Transfer*, vol. 46, no. 1, pp. 45–53, 2003. DOI: [10.1016/S0017-9310\(02\)00259-4](https://doi.org/10.1016/S0017-9310(02)00259-4).
- [35] S. Gacek and X. Wang, "Plume splitting in pico-second laser–material interaction under the influence of shock wave," *Phys. Lett. A*, vol. 373, no. 37, pp. 3342–3349, 2009. DOI: [10.1016/j.physleta.2009.07.044](https://doi.org/10.1016/j.physleta.2009.07.044).
- [36] C. Li, K. Burney, K. Bergler, and X. Wang, "Structural evolution of nanoparticles under picosecond stress wave consolidation," *Comput. Mater. Sci.*, vol. 95, pp. 74–83, 2014. DOI: [10.1016/j.commatsci.2014.07.036](https://doi.org/10.1016/j.commatsci.2014.07.036).
- [37] M. P. Allen and D. J. Tildesley, *Computer Simulation of Liquids*. Oxford: Clarendon Press, 1987.
- [38] S. Plimpton, "Fast parallel algorithms for short-range molecular dynamics," *J. Comput. Phys.*, vol. 117, no. 1, pp. 1–19, 1995. DOI: [10.1006/jcph.1995.1039](https://doi.org/10.1006/jcph.1995.1039).
- [39] X. Wang, "Large-scale molecular dynamics simulation of surface nanostructuring with a laser-assisted scanning tunnelling microscope," *J. Phys. D: Appl. Phys.*, vol. 38, no. 11, pp. 1805–1823, 2005. DOI: [10.1088/0022-3727/38/11/021](https://doi.org/10.1088/0022-3727/38/11/021).
- [40] X. Chen and X. Wang, "Near-field thermal transport in a nanotip under laser irradiation," *Nanotechnology*, vol. 22, no. 7, pp. 075204, 2011. DOI: [10.1088/0957-4484/22/7/075204](https://doi.org/10.1088/0957-4484/22/7/075204).
- [41] G. J. Keeler and D. N. Batchelder, "Measurement of the elastic constants of argon from 3 to 77°K," *J. Phys. C*, vol. 3, no. 3, pp. 510–522, 1970. DOI: [10.1088/0022-3719/3/3/004](https://doi.org/10.1088/0022-3719/3/3/004).
- [42] J. R. Morris and X. Song, "The melting lines of model systems calculated from coexistence simulation," *J. Chem. Phys.*, vol. 116, no. 21, pp. 9352–9358, 2002. DOI: [10.1063/1.1474581](https://doi.org/10.1063/1.1474581).
- [43] P. J. Steinhardt, D. R. Nelson, and M. Ronchetti, "Bond-orientational order in liquids and glasses," *Phys. Rev. B*, vol. 28, no. 2, pp. 784–805, 1983. DOI: [10.1103/PhysRevB.28.784](https://doi.org/10.1103/PhysRevB.28.784).
- [44] A. Stukowski, "Structure identification methods for atomistic simulations of crystalline materials," *Modell. Simul. Mater. Sci. Eng.*, vol. 20, no. 4, pp. 045021, 2012. DOI: [10.1088/0965-0393/20/4/045021](https://doi.org/10.1088/0965-0393/20/4/045021).